Materials Advances

ROYAL SOCIETY OF CHEMISTRY

PAPER

View Article Online
View Journal | View Issue

Cite this: *Mater. Adv.*, 2024, 5, 3735

A new thermoelectric Ag_8SiSe_6 argyrodite for room temperature application: sensitivity of thermoelectric performance to cooling conditions

Bo Wang,[a] Suwei Li,[a] Yubo Luo,[a] Junyou Yang,[a] Haitao Ye,*[b] Yong Liu*[c] and Qinghui Jiang*[a]

Received 31st December 2023,
Accepted 2nd March 2024

DOI: 10.1039/d3ma01190a

rsc.li/materials-advances

Current commercial thermoelectrics, like Bi_2Te_3-based compounds, generally include the expensive and toxic Te element, which hampers their large-scale thermoelectric applications in near room temperature conditions. In this work, a Ag_8SiSe_6 argyrodite compound, a new thermoelectric material as a potential candidate for Bi_2Te_3-based compounds, was fabricated by several synthesis processes. All the Ag_8SiSe_6-based thermoelectric bulks, exhibiting a density surpassing 95%, were successfully synthesized. The study investigated the impact of varying the quenching rate and techniques on Ag_8SiSe_6's thermoelectric performance. Our results revealed a pronounced relationship between the quenching parameters and pivotal thermoelectric metrics, including the Seebeck coefficient, electrical conductivity, and thermal conductivity. By optimizing the quenching conditions, we achieved a notable enhancement in *ZT* values, peaking over 0.7. This paves the way for Ag_8SiSe_6 to be considered as a competitive substitute for traditional n-type Bi_2Te_3-based compounds in thermoelectric applications under proximate room temperature conditions.

1 Introduction

Thermoelectric (TE) materials enable the conversion between thermal and electrical energy, a process of substantial importance for green energy harvesting and environmental protection.[1,2] The figure of merit *ZT*, a dimensionless constant, dictates the conversion efficiency of TE devices and is expressed as $ZT = S^2\sigma T/(\kappa_E + \kappa_L)$, where σ represents the conductivity, S is the Seebeck coefficient, κ_E is the electronic thermal conductivity, κ_L is the lattice thermal conductivity, T is the absolute temperature, and $S^2\sigma$ is defined as the power factor (PF). Total thermal conductivity (κ) can be written as $\kappa = \kappa_E + \kappa_L$. Clearly, an enhancement in the power factor coupled with a reduction in thermal conductivity is essential for improving the value of *ZT*.[3]

In recent years, several strategies, including modulation doping, inducing resonant levels, and band convergence, have been adopted to obtain higher electrical properties and power factors for relevant materials. These enhancements have been verified in SnSe,[4] PbTe,[5–7] Bi_2Te_3,[8] and BiCuSeO.[9] To optimize the thermal conductivity, strategies such as the incorporation of nano-inclusions, secondary phase recombination, and lattice anharmonicity have been introduced, and have been successfully applied to reduce the thermal conductivity of thermoelectric materials such as Bi_2Te_3,[10] $CoSb_3$,[11] Cu_3SbSe_4,[12] $AgSbTe_2$,[13] SnTe,[14] and Ag_8SnSe_6.[15]

At present, the commercial applications of thermoelectric materials are mainly focused on energy harvesting from the environment and solid-state cooling near room temperature.[16] For a long time, Bi_2Te_3-based alloys were the only material used in industrial thermoelectric modules for thermoelectric cooling in electronic equipment, large instrument cooling, and household cooling appliances.[17]

Research on superionic compounds revealed that these substances possess ultralow thermal conductivity and narrow band gaps.[18] These characteristics render superionic compounds as promising compounds to investigate for creating advanced thermoelectric materials with potential high *ZT* values.[19] Argyrodite compounds, recognized as promising thermoelectrics, have attracted considerable attention due to their significantly low lattice thermal conductivity.[20] This can be attributed to factors such as low sound velocity, complex crystal structure, liquid-like ions, and lattice anharmonicity. *Pei et al.*

[a] *State Key Laboratory of Materials Processing and Die and Mould Technology, and School of Materials Science and Engineering, Huazhong University of Science and Technology, Wuhan 430074, Hubei Province, China. E-mail: qhjiang@hust.edu.cn*
[b] *School of Engineering, University of Leicester, University Road, Leicester, LE1 7RH, UK. E-mail: haitao.ye@leicester.ac.uk*
[c] *Foshan (Southern China) Institute for New Materials, Foshan 528220, Guangdong Province, P. R. China. E-mail: liuy08@qq.com*

identified that the extremely low phonon velocity and small proportion of acoustic phonons in Ag_9AlSe_6 result in reduced thermal conductivity.[21] *Yang et al.* observed that the highly random ion occupancy in Ag_8SnSe_6 leads to soft bonding within the silver sub-lattice and phonon modes.[22]

Tremel *et al.* suggested that the thermal conductivity in Ag_8SiSe_6 is ameliorated by the high mobility and disorder of silver ions, thereby enhancing the thermoelectric properties of the material.[23] Our group reported that the nanoprecipitation of Ag_2Se and Si could further optimize the transport properties of Ag_2Se-Si-Ag_8SiSe_6 composite.[24] These two studies illuminated the potential of Ag_8SiSe_6 as a viable n-type candidate for the development of next-generation thermoelectric materials. Compounds from various groups have demonstrated a range of *ZT* values from 0.5 to 0.9.[23,24] However, there are scant details on the experimental processes for obtaining Ag_8SiSe_6 or related discussions about its purity. This raises a pertinent question: is the purity and stability of Ag_8SiSe_6 highly sensitive to the fabrication or cooling processing parameters? Such sensitivity could complicate the understanding of the material's intrinsic physical properties.

In this study, we thoroughly investigated the synthesis of Ag_8SiSe_6 compounds and successfully fabricated Ag_8SiSe_6-based thermoelectric bulks with a density exceeding 95%. We then delved deeper into the crystal structure, microstructure, and thermoelectric properties of these materials. A relationship was revealed between the cooling conditions, phase, microstructure, and their respective thermoelectric properties. After optimization of the fabrication processing parameters, the Ag_8SiSe_6 compounds, which exhibited a low thermal conductivity of 0.7 W m^{-1} K^{-1} and a high power factor surpassing 1200 μW m^{-1} K^{-2}, achieved a peak *ZT* of approximately 0.7 at 398 K.

2 Experimental

Synthesis of Ag_8SiSe_6

Polycrystalline Ag_8SiSe_6 ingots were synthesized using a high-temperature melting method with stoichiometric amounts of high-purity elements (> 99.99%) at 1223 K for 10 hours on quartz crucibles, which were subsequently cooled using different methods: cooling in a furnace (CF), quenching in air (QA), and quenching in water (QW). The resulting ingots were ground into powders and annealed at 773 K for 72 hours. Some quenched powders were additionally milled for 2 hours (QW&M). The final powders were hot-pressed under 60 MPa for 30 minutes to form pellets, achieving densities above 95% of the theoretical value.

Characterization

Pellet samples were ground into fine powder for X-ray diffraction (XRD) analysis (data collected on an XRD 7000 from Shimadzu Instrument at room temperature, using Cu Kα radiation with λ = 0.15418 nm). The fracture morphologies and compositional analyses of the bulk samples were conducted using field-emission scanning electron microscopy (FESEM, GeminiSEM300, Carl Zeiss), accompanied by energy-dispersive spectrometry.

Thermoelectric property measurements

The electrical resistivity ($\rho = 1/\sigma$) and Seebeck coefficient of the bulk samples were measured using a commercial Namicro III thermoelectric system, fabricated in the laboratory, with an uncertainty of 5%. The thermal conductivity (κ) was determined by the formula $\kappa = C_pD\lambda$, where the relative densities (D) were calculated using the Archimedes method, the specific heat capacity (C_p) was determined using the Dulong-Petit model, and the thermal diffusivity (λ) was assessed using the laser flash diffusivity method with LFA-427 (NETZSCH) equipment, with an uncertainty of 4%. Differential scanning calorimetry (DSC) measurements were performed using STA449F3 (NETZSCH) equipment at a heating rate of 5 K min^{-1}, and Hall measurements were conducted using an HMS 5500 Hall Effect measurement system under a 0.55 T magnetic field, employing the van der Pauw method.

3 Results and discussion

Fig. 1 presents the X-ray diffraction (XRD) patterns of the Ag_8SiSe_6 samples synthesized under various cooling conditions. The densities of these samples consistently exceed 95% of the theoretical value, a factor essential for optimizing the thermoelectric (TE) properties. The predominant diffraction peaks from the hot-pressed samples aligned with the $Pmn2_1$ space group, corroborating an earlier study by *Aversive et al.*[25] Additionally, certain diffraction peaks could be attributed to a secondary phase of Ag_2Se (PDF# 24-1041) characterized by the $P2_12_12_1$ space group.[26] Notably, as the cooling rate escalated, the intensity of the secondary phase (Ag_2Se) peaks diminished. This observation implies that high-temperature quenching facilitates the synthesis of Ag_8SiSe_6 and that rapid cooling can inhibit the generation of impurities, thus streamlining the subsequent annealing process to yield a more refined phase.

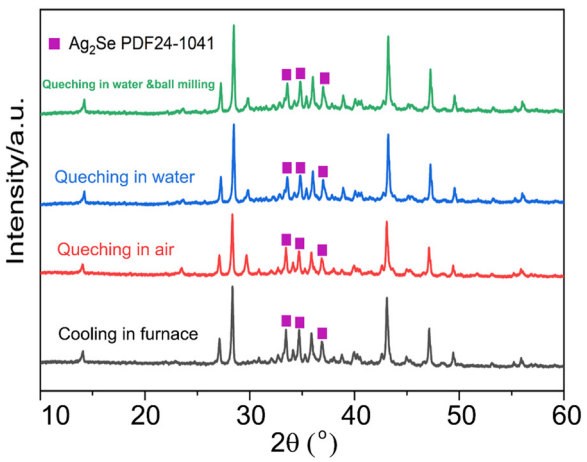

Fig. 1 XRD patterns of Ag_8SiSe_6 prepared under different quenching conditions.

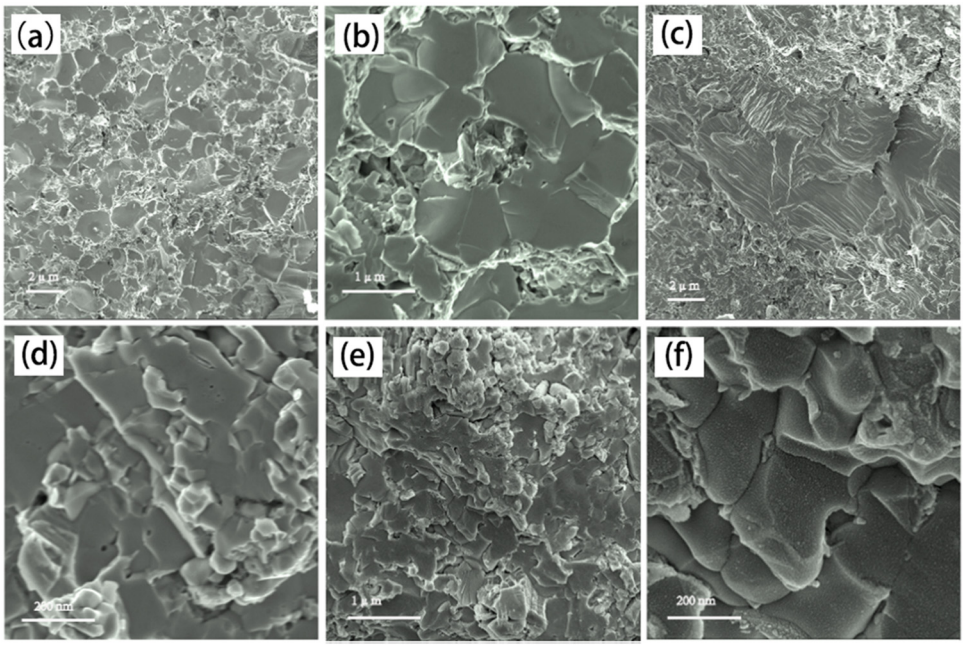

Fig. 2 (a) and (b) SEM fracture images of Ag_8SiSe_6 (cooling in furnace); (c) and (d) fracture morphologies of Ag_8SiSe_6 samples prepared with quenching in water; (e) and (f) fracture morphologies of Ag_8SiSe_6 (quenching in water) obtained with the ball-milling process.

However, the aforementioned results indicate that a pure Ag_8SiSe_6 phase cannot be prepared using the current methods.

Fig. 2 illustrates the fracture morphologies of Ag_8SiSe_6 bulk samples as revealed by scanning electron microscopy (SEM). The surface of the hot-pressed Ag_8SiSe_6, despite some discernible holes, appeared notably compact, corroborating the high density referred to earlier. As observed in the low-magnification SEM image in Fig. 2a, the grain diameter of Ag_8SiSe_6 (cooled in the furnace) varied between 2 and 3 μm. The medium-magnification SEM fracture image in Fig. 2b reveals complex grain boundaries and even some holes, potentially leading to increased material resistivity. Fig. 2c depicts the fracture morphologies of the Ag_8SiSe_6 samples quenched in water, exposing a cladding structure in which small grains enveloped larger ones. As shown in the high-magnification image in Fig. 2d, these small grains measured less than 500 nm and were nano-precipitates formed during quenching because the sample did not undergo ball milling.[27] This figure also reveals there was a reduction in porosity compared with previous samples. Fig. 2e shows a typical low-magnification SEM image of Ag_8SiSe_6 (quenched in water) following the ball-milling process, with grain sizes generally under 1 μm. Moreover, the high-resolution image in Fig. 2f's reveals a highly dense and uniform microstructure, conducive to lower resistivity. Nevertheless, ball milling may create additional defects and grain boundary surfaces, potentially impairing the electronic

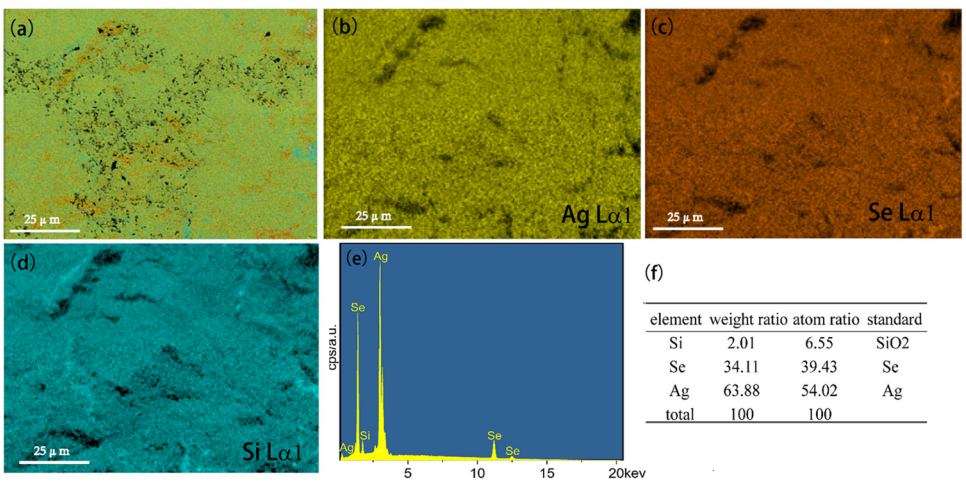

element	weight ratio	atom ratio	standard
Si	2.01	6.55	SiO2
Se	34.11	39.43	Se
Ag	63.88	54.02	Ag
total	100	100	

Fig. 3 EDS element analysis of the Ag_8SiSe_6 sample (quenching in water) obtained with the ball-milling process. (a) Hierarchical image of Ag_8SiSe_6; (b)–(d) compositional mapping of all elements; (e) and (f) composition analysis of Ag_8SiSe_6.

transport properties.[28] Therefore, optimal performance might be achieved through a judicious combination of these factors.

The microstructure of Ag_8SiSe_6 sample was evaluated using energy-dispersive spectrometry (EDS) for elemental analysis. Fig. 3a displays a hierarchical image of Ag_8SiSe_6, which encompasses all three constituent elements. The element distribution maps for Ag, Se, and Si are illustrated in Fig. 3b–d. Notably, the elements Ag, Se, and Si exhibited uniform distributions throughout the sample, devoid of any elemental clustering, a characteristic often observed in samples that undergo ball-milling treatment. To provide a deeper insight into the composition of the sample, a comprehensive analysis of the entire surface was performed. Fig. 3f presents the resultant data, delineating the weight ratio, atomic ratio, and standard sample measurements for all three elements. Through straightforward calculations, the actual atomic ratio for Ag, Si, and Se was determined to be approximately 8 : 1:6, affirming the successful synthesis of the primary Ag_8SiSe_6 phase.

Fig. 4a illustrates the temperature-dependent electrical resistivity of Ag_8SiSe_6 samples prepared under various conditions. The electrical resistivity of the samples cooled in the furnace (CF) and quenched in air (QA) exceeded that of the samples quenched in water (QW). In Fig. 4b, the Hall coefficient measurement revealed that the observed variations in resistivity mainly stemmed from a simultaneous increase in carrier concentration and mobility. This interesting phenomenon can be explained as a reduction of the second phase in the Ag-Si-Se alloy; whereby, according to the equation $8Ag + Si + 6Se \Rightarrow Ag_8SiSe_6 \Leftrightarrow 4Ag_2Se_{1+\delta} + (2 - 4\delta)Se + Si$, a reduction in the second phase would lead to decreased contents of Si and Se elements (although their low content and low crystalline mean they cannot be detected by XRD, as shown in Fig. 1). Since Si and Se have low a carrier concentration and mobility, their content reduction as second phases leads to low resistivity. After subjecting the samples to ball-milling treatment (QW&M), the electrical resistivity was slightly increased. Elemental analysis of the sample shown in Fig. 2f suggested that the milling process led to the creation of additional surfaces, defects, and stress, significantly contributing to the decrease in carrier concentration and mobility.

Fig. 4c illustrates the temperature dependence of the Seebeck coefficients of the Ag_8SiSe_6 samples, demonstrating that the room temperature Seebeck coefficients decreased with increasing the cooling rate. A corresponding downward trend in the measured carrier concentration was also noticeable. Fig. 4d depicts the relationship between the room temperature Seebeck coefficient and carrier concentration in accordance with Pisarenko's theory, further indicating a decrease in the effective mass m^*. Herein, the single parabolic band (SPB) model was used to calculate the Pisarenko plot related to the Seebeck coefficient and carrier concentration according to the following equations:[29]

$$n = \frac{(2m_d^* k_B T)^{3/2}}{2\pi^2 \hbar^3} F_{1/2}(\eta) \quad (1)$$

$$r_H = \frac{3}{4} \frac{F_{1/2}(\eta) F_{-1/2}(\eta)}{F_0(\eta)^2} \quad (2)$$

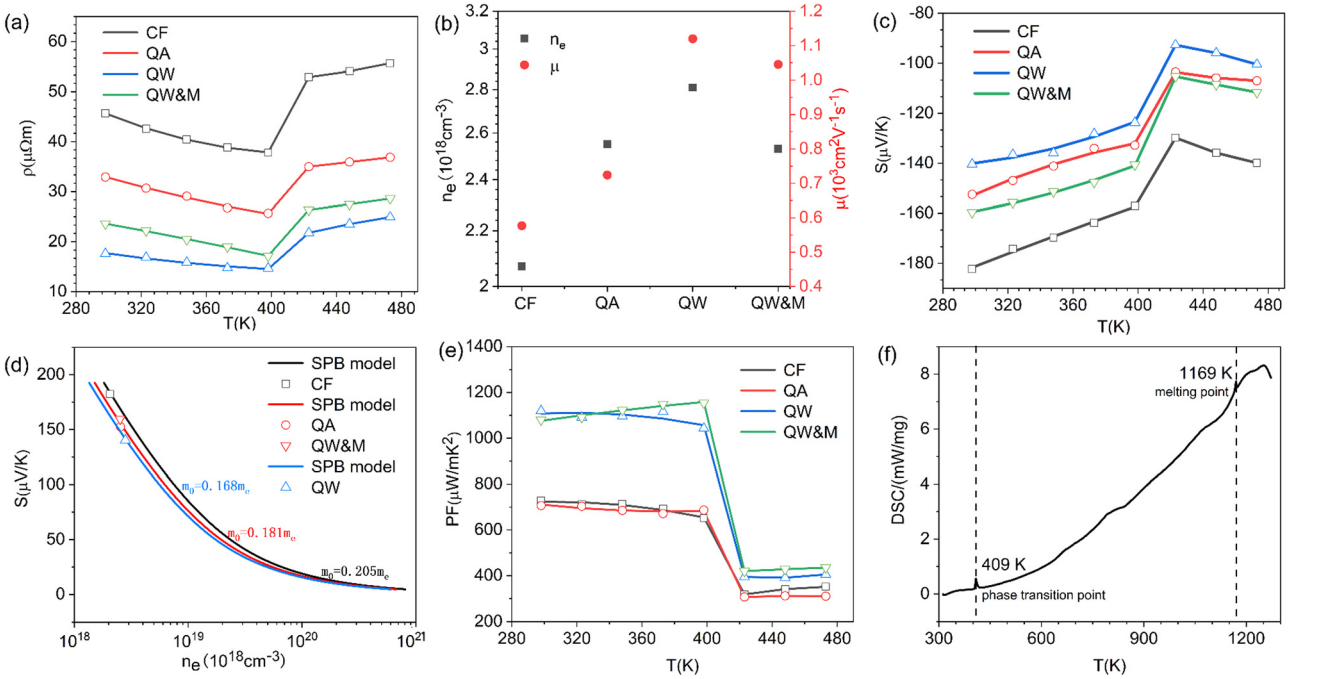

Fig. 4 (a) Electrical resistivity dependence on temperature; (b) Hall mobility and Hall carrier concentration dependence on different treatments; (c) Seebeck coefficient dependence on temperature; (d) room temperature Seebeck coefficient as a function of carrier concentration based on the Pisarenko relationship; (e) Power factor dependence on temperature; (f) differential scanning calorimetry (DSC) measurement of Ag_8SiSe_6.

$$s = \frac{k_B}{e}\left(\left[\frac{2F_1(\eta)}{F_0(\eta)} - \eta\right]\right) \quad (3)$$

$$F_x(\eta) = \int_0^\infty \frac{\varepsilon^x}{1+\exp(\varepsilon-\eta)}\mathrm{d}\varepsilon \quad (4)$$

where $F_x(\eta)$ is the Fermi integral, η is the reduced Fermi energy, r_H is the Hall factor, h is the Planck constant, k_B is the Boltzmann constant, and m^* is the total density of the effective mass of the states. Because the Seebeck coefficient is intimately connected to m^*, an enhanced Seebeck coefficient correlates with an increased m^*. Additionally, the Seebeck coefficient, as seen in Fig. 4c, underwent a sharp change around 400 K, marking a phase transition at this temperature.

Regarding the calculated power factor (PF = $(1/\rho)S^2$), the data were assembled and a graph plotted, as shown in Fig. 4e. All four samples exhibited similar trends, with their power factors remaining relatively stable until the phase-transition temperature. Notably, the PF of the QW sample was sharply augmented across the entire measurement temperature range. Upon the introduction of ball milling, the power factor escalated with increasing the temperature before 400 K, reaching a maximum value of approximately 1200 μW m^{-1} K^{-2} at 398 K in the QW&M sample.

The results from the differential scanning calorimetry (DSC) analysis of Ag_8SiSe_6 powder are presented in Fig. 4f. The peak value of 409 K is considered indicative of a phase-transition temperature during the first-order structural transition. For Ag–Si–Se compounds, this peak can only be attributed to the contribution of the phase transition of Ag_2Se and Ag_8SiSe_6. *Wang et al.*[30] and *Mi et al.*,[31] respectively, reported there is a peak near 400 K consistent with the phase-transition temperature of Ag_2Se compounds. Meanwhile, *Tremel et al.*[23] identified that this peak was consistent with the phase transition occurring near 400 K in Ag_8SiSe_6, a representative of the argyrodite compounds. Above this temperature, Ag_8SiSe_6 exhibits a face-centered cubic structure in which Ag^+ cations are fully disordered in the $[SiSe_6]^{8-}$ anion sublattice, comprising Se^{2-} anions and $[SiSe_4]^{4-}$ units. Below this temperature, Ag_8SiSe_6 exhibits an orthorhombic structure with a space group $Pmn2_1$, transforming to a cubic structure with the space group $F\bar{4}\bar{3}m$ at elevated temperatures.[32,33] As a result, Ag^+ cations are partially localized, leading to a reduction in electrical conductivity and an increase in Seebeck coefficients.

Similar semiconductor-superionic conductor phase transitions were reported in the Ag_2Se system by *Xie et al.*[34] These insights suggest a novel and effective approach to enhancing the thermoelectric power factor is by capitalizing on the abnormal electrical transport characteristics near the phase-transition temperature.

The thermal diffusivity coefficient λ and specific heat C_p are illustrated in Fig. 5a and b, respectively. The thermal conductivity κ was derived using the equation $\kappa = DC_p\lambda$, and is presented in Fig. 5c (in order to avoid the argued abnormal behaviour in ZT like Cu_2Se,[35] the sharp peak near 400 K was ignored in the specific heat curve during the calculation of the

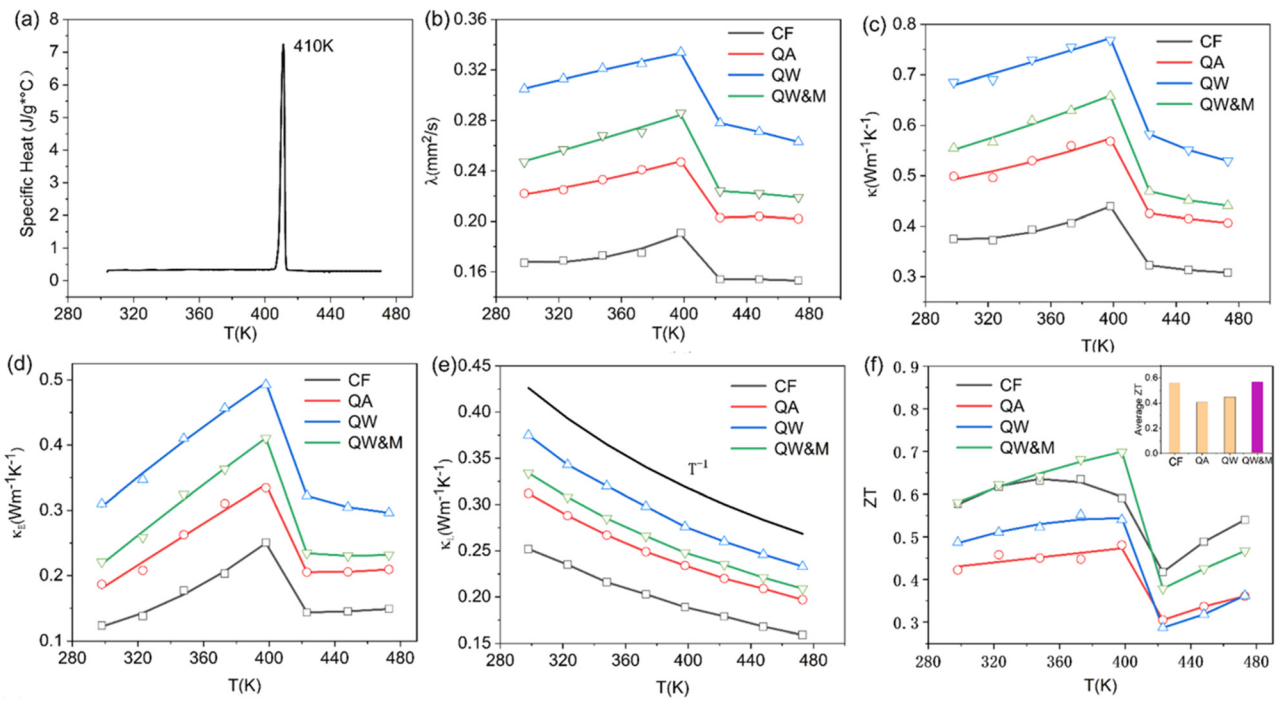

Fig. 5 (a) Temperature-dependent specific heat; (b) temperature-dependent thermal diffusivity coefficient; (c) total thermal conductivities κ dependence on the temperature of different treatments; (d) electronic thermal conductivity dependence on temperature; (e) lattice thermal conductivity dependence on temperature; (f) ZT values as a function of temperature.

thermal conductivity). With the increase in temperature, the thermal conductivity first exhibited a slight rise followed by a notable decline. Data points for κ across all the samples predominantly ranged between 0.3 and 0.8 W m^{-1} K^{-1} throughout the temperature spectrum. Such exceptionally low thermal conductivity[36] has also been observed in other argyrodite compounds and can be attributed to factors such as low sound velocity, intricate crystal structures, liquid-like ions, and lattice anharmonicity.[37]

The electronic thermal conductivity, calculated using the Wiedemann–Franz law ($\kappa_E = LT/\rho$), is depicted in Fig. 5d. Here, L represents the Lorenz factor as determined by the single parabolic band (SPB) model in conjunction with acoustic scattering.[38,39] The lattice thermal conductivity can then be deduced by subtracting the electronic thermal conductivity from the total thermal conductivity, as shown in Fig. 5e. A discernible linear relationship existed between κ_L and T^{-1}, indicating that Umklapp scattering was the primary phonon mechanism. Furthermore, the lattice thermal conductivity reached a low of around 0.17 W m^{-1} K^{-1}, a phenomenon likely resulting from the high disordering of soft bonding, Ag ions, and the low cut-off frequency of acoustic phonons.[40] This value was consistent with the values for Ag_8SiSe_6 compounds published by other reports in literatures[23,24] and is also one of the lowest values of lattice thermal conductivities (for example, see 0.12 W m^{-1} K^{-1} at 300 K for Ag_9GaSe_6,[41] and 0.13 W m^{-1} K^{-1} for Ag_8SnSe_6[42]). However, it is counterintuitive that the phase transition does not affect κ_L. The lack of a proper explanation for this phenomenon makes it an open question that requires further exploration.

ZT values are plotted in Fig. 5f, with the average *ZT* values featured in the inset. The combination of quenching and ball-milling treatment optimized the temperature-dependent *ZT* and average *ZT* values across the entire temperature range. A peak *ZT* value of approximately 0.71 was attained at 398 K in the QW&M sample, primarily stemming from the combined effect of a high power factor exceeding 1200 μW m^{-1} K^{-2} and a reduced lattice thermal conductivity. This value is similar to those reported in literature.[23,24] The highest average *ZT*, around 0.57, was observed in the QW&M sample at 398 K (inset of Fig. 5f).

4 Conclusions

Thermoelectric bulks based on Ag_8SiSe_6 were synthesized through a traditional melting process combined with a hot pressing method, marking the first systematic investigation of their thermoelectric properties linked to different post-treatments. By varying the cooling rates of the ingots, a substantial improvement in the power factor was attained, particularly in the sample quenched in water, due to a marked reduction in resistivity. Although a pure Ag_8SiSe_6 phase could not be prepared using the current methods, a high-performance thermoelectric material was fabricated through the integration of ball-milling treatment with the quenched ingot, achieving a peak *ZT* value of approximately 0.71 at 398 K. Further research is warranted to understand the underlying mechanisms and optimize the material for commercial applications.

Conflicts of interest

There are no conflicts to declare.

Acknowledgements

This work was supported by the National Natural Science Foundation of China (52273293, 52172187, 51772019, and 51572098).

References

1 S. Y. Tee, D. Ponsford, C. L. Lay, X. Wang, X. Wang, D. C. J. Neo, T. Wu, W. Thitsartarn, J. C. C. Yeo, G. Guan, T.-C. Lee and M.-Y. Han, *Adv. Sci.*, 2022, **9**, 2204624.
2 Q. Jiang, J. Yang, P. Hing and H. Ye, *Mater. Adv.*, 2020, **1**, 1038–1054.
3 B. Cai, H. Hu, H.-L. Zhuang and J.-F. Li, *J. Alloys Compd.*, 2019, **806**, 471–486.
4 X. Zhang, J. Cai, X. Tan, S. Zhuang, W. Huang, Z. Zhang, H. Hu, J. Wu, G.-Q. Liu and J. Jiang, *Mater. Adv.*, 2023, **4**, 1372–1377.
5 K. Zhang, H. Wang, W. Su, T. Wang, X. Wang, T. Chen, T. Huo, F. Dang, M. Dong, C. Wang, B. Dong and Z. Guo, *J. Phys. D: Appl. Phys.*, 2020, **53**, 245501.
6 T. Chen, K. Zhang, H. Wang, W. Su, F. Mehmood, T. Wang, J. Zhai, X. Wang, T. Huo and C. Wang, *J. Mater. Chem. C*, 2020, **8**, 1679–1685.
7 M. Huang, P. Zhai, S. I. Morozov, W. A. Goddard, G. Li and Q. Zhang, *J. Alloys Compd.*, 2023, **959**, 170429.
8 Y. Cheng, J. Yang, Y. Luo, W. Li, A. Vtyurin, Q. Jiang, S. Dunn and H. Yan, *ACS Appl. Mater. Interfaces*, 2022, **14**, 37204–37212.
9 W. Tang, W. Ma, P. Yu, Z. Zhou, J. Lan, Y.-H. Lin and X. Yang, *Mater. Today Phys.*, 2022, **28**, 100898.
10 Q. Jiang, J. Yang, J. Xin, Z. Zhou, D. Zhang and H. Yan, *J. Alloys Compd.*, 2017, **694**, 864–868.
11 B. Popescu, M. Galatanu, M. Enculescu and A. Galatanu, *J. Alloys Compd.*, 2022, **893**, 162400.
12 D. Xie, B. Zhang, A. Zhang, Y. Chen, Y. Yan, H. Yang, G. Wang, G. Wang, X. Han, G. Han, X. Lu and X. Zhou, *Nanoscale*, 2018, **10**, 14546–14553.
13 M. Yan, X. Tan, Z. Huang, G. Liu, P. Jiang and X. Bao, *J. Mater. Chem. A*, 2018, **6**, 8215–8220.
14 X. Liu, B. Zhang, Y. Chen, H. Wu, H. Wang, M. Yang, G. Wang, J. Xu, X. Zhou and G. Han, *ACS Appl. Mater. Interfaces*, 2020, **12**, 44805–44814.
15 W. Li, S. Lin, B. Ge, J. Yang, W. Zhang and Y. Pei, *Adv. Sci.*, 2016, **3**, 1600196.

16 Z. Han, J.-W. Li, F. Jiang, J. Xia, B.-P. Zhang, J.-F. Li and W. Liu, *J. Materiomics*, 2022, **8**, 427–436.
17 Q. Jiang, D. Pan, Y. Wang, Y. Liu, Y. Luo, J. Yang, B. Li, S. Dunn and H. Yan, *Small*, 2024, **20**, 2306786.
18 T. P. Bailey and C. Uher, *Curr. Opin. Green Sustainable Chem.*, 2017, **4**, 58–63.
19 H. Hu, K. Xia, T. Zhu and X. Zhao, *Chin. J. Rare Met.*, 2021, **45**, 513–529.
20 C. Yang, Y. Xia, L. Xu, Y. Luo, X. Li, Z. Han and J. Cui, *Chem. Eng. J.*, 2021, **426**, 131752.
21 W. Li, S. Lin, M. Weiss, Z. Chen, J. Li, Y. Xu, W. G. Zeier and Y. Pei, *Adv. Energy Mater.*, 2018, **8**, 1800030.
22 C. Yang, Y. Luo, X. Li and J. Cui, *RSC Adv.*, 2021, **11**, 3732–3739.
23 B. K. Heep, K. S. Weldert, Y. Krysiak, T. W. Day, W. G. Zeier, U. Kolb, G. J. Snyder and W. Tremel, *Chem. Mater.*, 2017, **29**, 4833–4839.
24 Q. Jiang, S. Li, Y. Luo, J. Xin, S. Li, W. Li, G. Zhao and J. Yang, *ACS Appl. Mater. Interfaces*, 2020, **12**, 54653–54661.
25 I. J. Alverdiev, S. M. Bagheri, Z. M. Aliyeva, Y. A. Yusibov and M. B. Babanly, *Inorg. Mater.*, 2017, **53**, 786–796.
26 C. Xiao, J. Xu, K. Li, J. Feng, J. Yang and Y. Xie, *J. Am. Chem. Soc.*, 2012, **134**, 4287–4293.
27 L. L. Zhao, X. L. Wang, J. Y. Wang, Z. X. Cheng, S. X. Dou, J. Wang and L. Q. Liu, *Sci. Rep.*, 2015, **5**, 7671.
28 L. Hu, T. Zhu, X. Liu and X. Zhao, *Adv. Funct. Mater.*, 2014, **24**, 5211–5218.
29 D. Zhang, J. Yang, Q. Jiang, Z. Zhou, X. Li, J. Xin, A. Basit, Y. Ren, X. He, W. Chu and J. Hou, *ACS Appl. Mater. Interfaces*, 2017, **9**, 28558–28565.
30 J. L. Wang, W. L. Fan, J. Yang, Z. L. Da, X. F. Yang, K. M. Chen, H. Yu and X. N. Cheng, *Chem. Mater.*, 2014, **26**, 5647–5653.
31 W. Mi, P. Qiu, T. Zhang, Y. Lv, X. Shi and L. Chen, *Appl. Phys. Lett.*, 2014, **104**, 133903.
32 X. Shen, C.-C. Yang, Y. Liu, G. Wang, H. Tan, Y.-H. Tung, G. Wang, X. Lu, J. He and X. Zhou, *ACS Appl. Mater. Interfaces*, 2018, **11**, 2168–2176.
33 E. Gaudin, F. Boucher, M. Evain and F. Taulelle, *Chem. Mater.*, 2000, **12**, 1715–1720.
34 C. Xiao, J. Xu, K. Li, J. Peng, J. Yang and Y. Xie, *J. Am. Chem. Soc.*, 2012, **134**, 4287–4293.
35 D. Byeon, R. Sobota, K. Delime-Codrin, S. Choi, K. Hirata, M. Adachi, M. Kiyama, T. Matsuura, Y. Yamamoto, M. Matsunami and T. Takeuchi, *Nat. Commun.*, 2019, **10**, 72.
36 E. Deligoz, H. Ozisik and E. Bolen, *Inorg. Chem. Commun.*, 2022, **142**, 109689.
37 C. Chang and L. D. Zhao, *Mater. Today Phys.*, 2018, **4**, 50–57.
38 K. S. Weldert, W. G. Zeier, T. W. Day, M. Panthofer, G. J. Snyder and W. Tremel, *J. Am. Chem. Soc.*, 2014, **136**, 12035–12040.
39 J. Xin, J. Yang, S. Li, A. Basit, B. Sun, S. Li, Q. Long, X. Li, Y. Chen and Q. Jiang, *Chem. Mater.*, 2019, **31**, 2421–2430.
40 S. Lin, W. Li, S. Li, X. Zhang, Z. Chen, Y. Xu, Y. Chen and Y. Pei, *Joule*, 2017, **1**, 816–830.
41 B. Jiang, P. Qiu, H. Chen, J. Huang, T. Mao, Y. Wang, Q. Song, D. Ren, X. Shi and L. Chen, *Mater. Today Phys.*, 2018, **5**, 20–28.
42 Z. H. Yu, X. X. Wang, C. Y. Liu, Y. R. Cheng, Z. W. Zhang, R. F. Si, X. B. Bai, X. K. Hu, J. Gao, Y. Peng and L. Miao, *J. Adv. Ceram.*, 2022, **11**, 1144–1152.